

INITIATION AND DEVELOPMENT OF THE WHITE-LIGHT AND RADIO CME ON 15 APRIL 2001

P. DÉMOULIN¹, A. VOURLIDAS², M. PICK¹, A. BOUTEILLE¹

Draft version March 12, 2012

ABSTRACT

The 2001 April 15 event was one of the largest of the last solar cycle. A former study (Maia et al., 2007) established that this event was associated with a coronal mass ejection (CME) observed both at white light and radio frequencies. This radio CME is illuminated by synchrotron emission from relativistic electrons. In this paper, we investigate the relation of the radio CME to its extreme ultraviolet (EUV) and white light counterpart and reach four main conclusions. i) The radio CME corresponds to the white light flux rope cavity. ii) The presence of a reconnecting current sheet behind the erupting flux rope is framed, both from below and above, by bursty radio sources. This reconnection is the source of relativistic radiating electrons which are injected down along the reconnected coronal arches and up along the flux rope border forming the radio CME. iii) Radio imaging reveals an important lateral over expansion in the low corona; this over expansion is at the origin of compression regions where type II and III bursts are imaged. iv) Already in the initiation phase, radio images reveal large scale interactions of the source active region with its surroundings, including another active region and open magnetic fields. Thus, these complementary radio, EUV, white light data validate the flux rope eruption model of CMEs.

Subject headings: Sun: corona — Sun: coronal mass ejections (CMEs) — Sun: flare — Sun: radio radiation — Sun: X-rays, gamma rays

1. INTRODUCTION

Coronal Mass Ejections (CMEs) are large-scale eruptive events that originate close to the solar surface and are accelerated in the inner corona. CMEs are often associated with eruptive prominences or with the disappearance of filaments. CMEs seen in coronagraph images, typically contain three distinct regions: a bright core, surrounded by a dark cavity, surrounded itself by a bright compression front (Illing & Hundhausen 1986; Subramanian & Vourlidas 2007; Patsourakos, Vourlidas, and Kliem 2010, and references therein). Based on the velocity profile of CMEs, Zhang et al. (2001) described the evolution of CMEs into three distinct stages: an initiation phase of slow ascension of the magnetic configuration, an impulsive phase of rapid increase of the mean velocity and CME expansion and a propagation phase with nearly constant velocity or a smooth deceleration. There is also a good correlation between CME acceleration profiles and time derivative of the soft X-ray profiles (Zhang and Dere 2006; Maričić et al. 2007).

The standard picture of a CME eruption involves an initially closed and stressed magnetic configuration which becomes unstable and erupts. Most CMEs models agree that the final ejected structure is a magnetic flux rope. In that case, the cavity seen in white light, or the emission void observed in EUV, correspond to an expanding flux rope (e.g. Chen et al. 1997; Thernisien et al. 2009). A flux rope is expected to be already present during the emergence phase of active regions (ARs) since the trace of the azimuthal field component is observed as magnetic tongues which resemble the “yin-yang” pattern

in photospheric magnetograms (Luoni et al. 2011). However, a flux rope typically cannot cross the photosphere directly. Rather, it is transformed by magnetic reconnection, and a smaller flux rope is formed which can finally enter in the corona (Hood et al. 2009, and references therein). A coronal flux rope can also be formed during the decay phase of an AR from a sheared arcade. The key physical ingredient is the dispersion of the photospheric magnetic field due to the convection. This induces magnetic cancellation in the vicinity of the magnetic inversion line and transforms progressively a sheared arcade to a flux rope. Green et al. (2011) provided detailed observational evidences of such photospheric cancellation, which built up progressively an X-ray sigmoid and finally lead to a CME. These results are in agreement with the 3D magneto-hydrodynamic (MHD) simulation of the formation, then eruption, of a flux rope due to shearing motions and diffusion at the photospheric level (Aulanier et al. 2010).

Field lines passing above the flux rope are stretched during the eruption, and a current sheet (CS) is formed below the flux rope and above the photospheric magnetic inversion line (see e.g. Forbes et al. 2006, and references therein). Then, magnetic reconnection occurs along this current sheet: first at low altitudes, then at progressively greater heights. This reconnection builds up the flux rope further. The early consequence of this reconnection is observed sometimes as the transformation of two sets of J-shaped coronal loops into a set of reconnected loops (flare loops) and another set of sigmoidal loops (Liu et al. 2010, and references therein). Independently, 3D MHD simulations show the same processes (Amari et al. 2010, and references therein). Detailed observations of SDO confirm these processes, and show that the erupting flux rope can be very hot ($T \approx 10$ MK, Cheng et al. 2011). Hence, at lower temperatures (around 1 MK), the flux rope area appears as a cavity surrounded by stretched

Electronic address: Pascal.Demoulin@obspm.fr

¹ LESIA, UMR 8109 CNRS, UPMC, Université Paris-Diderot, Observatoire de Paris-Meudon, Meudon, 92195, France

² Space Sciences Division, Naval Research Laboratory, Washington, DC 20375, USA

loops which are observed to have a converging motion below the flux rope. This flow is expected to further feed magnetic reconnection below the flux rope, and indeed shrinking flare loops are observed below this region. Still, the eruption could be fast enough that fast magnetic reconnection cannot avoid the build up of a long CS (Lin & Forbes 2000). Indeed, there have been several reports, from UV and X-rays observations, of straight structures interpreted as CS present in the wake of CMEs (see Ciavarella & Raymond 2008; Vršnak et al. 2009; Saint-Hilaire et al. 2009, and references therein). The above summary of the global characteristics of CMEs is in close agreement with MHD models (see e.g. Forbes et al. 2006; Chen 2011, and references therein).

Cohen et al. (2010) underlined that the interaction with the complex ambient environment might significantly affect the propagation of the CME. Indeed, many large flare-associated CME events have a much more complex configuration than the three part structure. Radio images of fast/flare CME events show that they reach their full extension in a few minutes through successive magnetic interactions with neighbored coronal structures (e.g. Maia et al. 1999). The opening of the CME loops, or at least the transformation to large scale, by successive reconnections with open or large scale loops, leave a wide-spread dimmed region in EUV (e.g. Pohjolainen et al. 2001; Attrill et al. 2007; Mandrini et al. 2007; Pick & Vilmer 2008, and reference therein).

In addition to space-based observations, radio spectral and imaging observations are obtained with extremely high time resolution and sample different heights in the solar atmosphere. So they contribute significantly in our understanding of CME initiation and development as briefly summarized below. During the initiation phase, non-thermal radio bursts are detected and are the signature of electron beams accelerated during the early magnetic field interactions (Pick & Vilmer 2008, and reference therein). The first indications of CSs in the solar corona were provided by radio spectral observations. Kliem et al. (2000) observed long series of quasi-periodic pulsations deeply modulating a continuum in the 0.62 GHz range that was slowly drifting toward lower frequencies. They proposed a model in which the pulsations of the radio flux are caused by quasi-periodic particle acceleration episodes that result from a dynamic phase of magnetic reconnection in a large-scale current sheet (see also Karlický et al. 2004). Pick et al. (2005) traced the imaging dynamical evolution of the reconnecting CS behind an ejected flux rope and provided an upper estimate of the CS length from the position of the observed pair of radio sources (consisting of an almost stationary and a fast moving sources). Then, Aurass et al. (2009) provided a diagnosis of the presence of a CS in the aftermath of a CME both with X-ray and radio spectral observations. Finally, Huang et al. (2011) demonstrated that joint imaging radio and extreme-ultraviolet observations can trace the extent and orientation of the flux rope and its interaction with the surrounding magnetic field. This allows to characterize in space and time the processes involved in the CME launch.

Bastian et al. (2001) first reported the existence of an ensemble of expanding loop-like structures that were imaged at radio wavelengths by the Nançay Radioheliograph (NRH). These loops were detected until a helio-

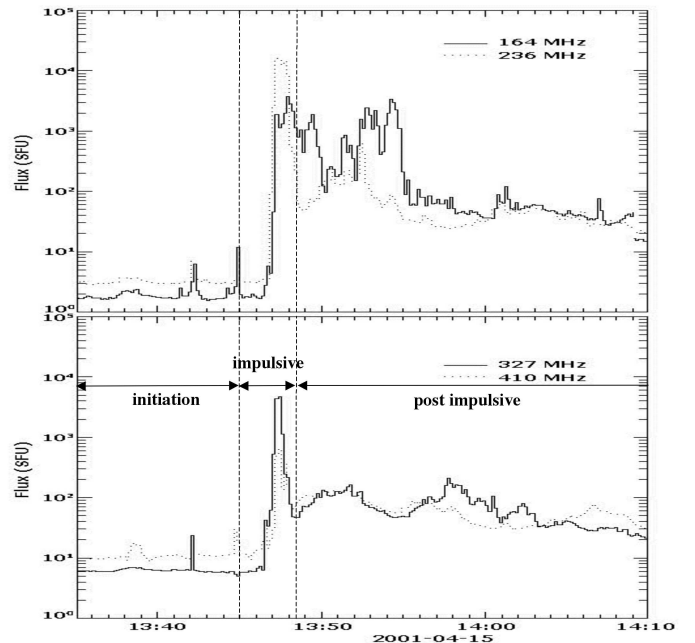


FIG. 1.— Flux evolution measured at four frequencies by the NRH: we distinguish the weak early activity, the strongest peak in the impulsive phase and two successive outbursts at 164 MHz (flux peaks).

centric distance of $3 R_{\odot}$ (solar radius) and were located behind the front of the white light CME on 1998 April 20. The faint emission of these loops, named *radio CME*, was attributed to incoherent synchrotron radiation from 0.5-5 MeV electrons spiraling within a magnetic field ranging from 0.1 to a few Gauss. Following this discovery, Maia et al. (2007) identified another radio CME, on 2001 April 15, which was one of the strongest solar energetic particle event of the last solar cycle, associated to a ground level enhancement (GLE) detected with neutron monitors, even if it was not a well connected to Earth by the Parker spiral (because it was a limb event, Masson et al. 2012a).

In this paper, we further analyze the 2001 April 15 CME. It provides an almost unique opportunity to investigate the formation and early development of a CME through its associated radio sources, as well as its link with the white light CME. The radio data analysis is presented in Section 2. This section starts with an overview of the event which leads us to distinguish successive phases which are described in separated subsections. Then, Section 3 presents a comparison of the radio CME to the LASCO images. The close kinematical and morphological similarities between the radio and white light CME strongly suggest that the radio CME corresponds to the flux rope seen from a side point of view. Finally, we discuss the physical implications of our results in Section 4 and we conclude in Section 5.

2. RADIO OBSERVATIONS

2.1. Overview

The radio images are provided by the multifrequency Nançay Radioheliograph, NRH, (Kerdron & Delouis 1997). The radio spectral data are obtained by the

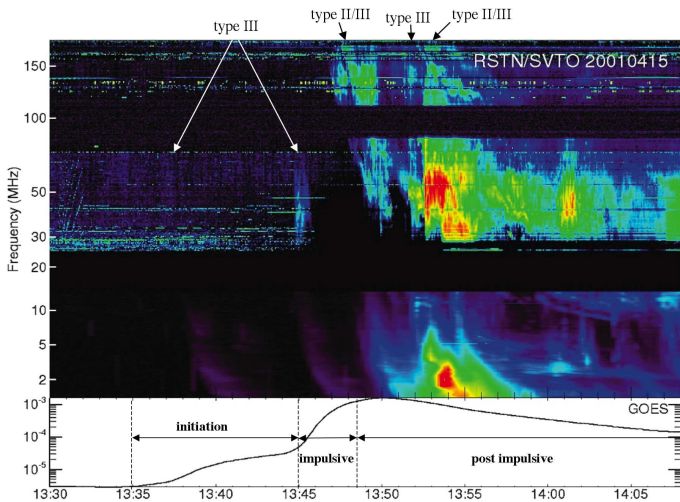


FIG. 2.— *Upper panel*: composite spectrum from San-Vito and WIND/WAVES data, obtained from http://www.astro.umd.edu/~rduffin/one_hour_plots/TYPE_IIs/-20010415_1330_ (original data are at ftp://ftp.ngdc.noaa.gov/STP/SOLAR_DATA/SOLAR_RADIO/). The flux is coded from negligible flux or missing data in black to strong flux in red. The three band of frequencies are calibrated independently. *Lower panel*: soft X-ray flux at 1-8 Å from GOES.

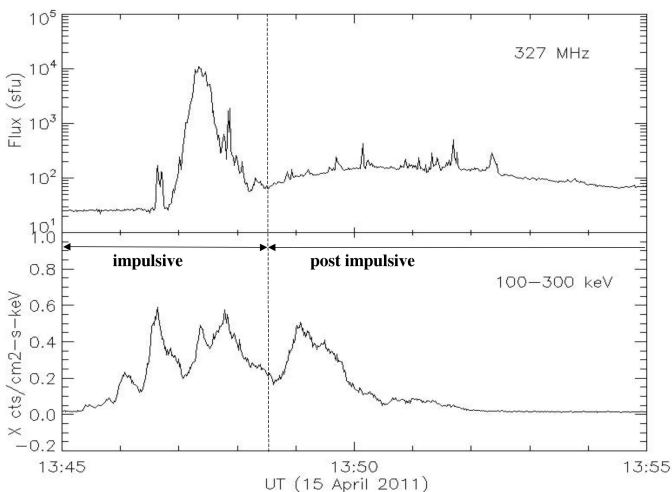


FIG. 3.— *Upper pannel*: temporal evolution of the radio flux measured at 327 MHz with an integration time of one second. Following the impulsive phase, after 13:48:30 UT, the radio emission exhibits a series of short duration bursts superimposed on a smooth continuum. *Lower pannel*: hard X-ray flux measured by GOES in the energy range 100-300 keV.

RSTN/San-Vito spectrograph (180-25 MHz)³ and by the WAVES radio receiver on the WIND spacecraft (13.8-0.30 MHz Bougeret et al. 1995). We used the EUV and white light imaging observations from the Extreme ultraviolet Imaging Telescope (EIT) and the Large Angle and Spectrometric Coronagraph (LASCO) images both aboard the Solar and Heliospheric Observatory (SOHO) (Brueckner et al. 1995; Delaboudinière et al. 1995).

An overview of the time evolution of the radio fluxes is shown in Figure 1, while Figure 2 displays a composite radio spectrum and the time profile of the soft X-ray flux. We define three phases according to the behavior of the radio emissions, complemented with the soft X-ray flux.

³ <http://www.astro.umd.edu/~rduffin/>

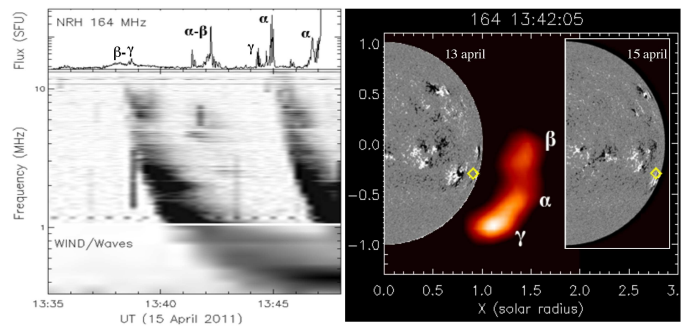


FIG. 4.— *Pre-eruptive activity*. *Right panel*: type III bursts detected at 164 MHz and at kilometric wavelengths (stronger flux is darker). The labels α , β and γ identify the radio sources on the radio image. *Left panel*: MDI magnetograms on April 13 and sources at 164 MHz of pre-eruptive activity on April 15. The location of the flare is indicated by a yellow diamond in this and following figures. A MDI magnetogram on April 15 is added on the right side showing that the CME source region is at the limb at the CME launch time.

A first period of pre-eruptive activity, the *initiation phase*, is characterized by a weak activity at radio and soft X-ray wavelengths (Figures 1, 2). Already during this phase the observed radio sources have a broad lateral extent and some are associated with interplanetary (IP) type III bursts (Figures 2, 4).

The onset of the next period, the *impulsive phase*, is marked by the occurrence of a type III burst at 13:44:45 UT (Figure 2) and by a GOES X14 flare starting at 13:45 UT and peaking at 13:49 UT. Hard X-ray intense peaks are also present during this phase (Figure 3). A radio source, called A_i , is observed at the three highest NRH frequencies reported in Figure 1 and is imaged in Figure 5. This source has two components: one has a smooth flux evolution while the other one is rapidly evolving. Near the end of this period, a type II/III burst is detected at meter and lower wavelengths (Figure 2). The event was also associated with energetic hard X-ray (HXR) and γ -ray emissions (Tyka et al. 2003).

Finally, the *post-impulsive phase* is characterized at its beginning by a smooth continuum with a series of short duration bursts superimposed (Figure 3). These characteristics are used to define the post-impulsive phase, even if a last hard X-ray peak is observed at its beginning (with similar flux evolution than the others peaks in the impulsive phase, Figure 3). This phase is also characterized by the rapid outward motion of the previous source A_i , now called A, as well as the appearance of new radio sources, B and C, which first detached backward from source A, then they stay behind and have a lower speed than source A (see Section 2.4 and Figure 6). Finally, in the latest phase of the event, the radio sources reveal a southern expansion of the CME.

To clarify the link between the development of these successive phases and the evolution of the radio CME, the positions of several sources which illustrate the time sequence of the event, are overplotted on images of the radio CME from Maia et al. (2007) in Figures 7 and 9. Note that the images in these figures were saturated in order to reveal the weak emission of the radio CME.

2.2. Initiation Phase (13:35 - 13:45 UT)

This phase is characterized by the progressive increase of soft X-ray flux (Figure 2, bottom panel), by the occurrence of a few weak bursts at 164 MHz (Figure 1,

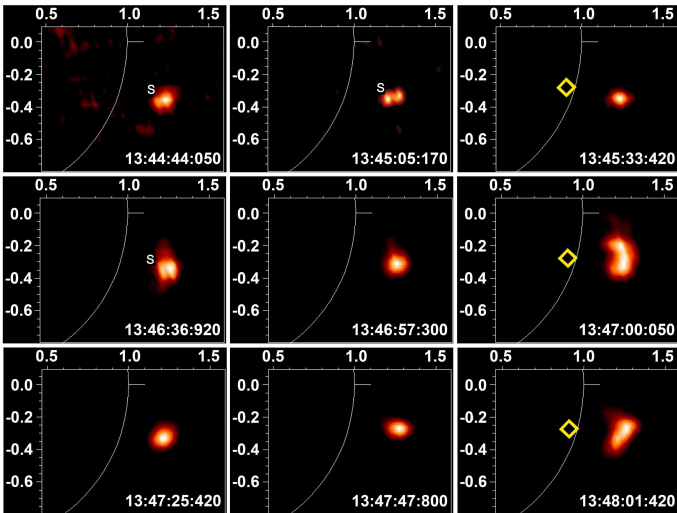


FIG. 5.— *Impulsive phase*: snapshots of the emitting region at 410 MHz, called globally source A_i and formed of two components. Label 'S' indicates the sporadic source of the short duration bursts (see Section 2.3), while the other source is a more stable component, responsible for the continuum emission.

upper panel) and by the presence of IP type III bursts (Figures 2 and 4, left panel).

The CME is launched from AR 9415 which has a complex photospheric magnetic field ($\beta\gamma\delta$ configuration). The large-scale main bipole of this AR has the leader (negative) polarity tilted towards the equator and with the same magnetic polarity as dominantly present in the southern hemisphere for this solar cycle. Except for its magnetic complexity, the source AR is a classical large AR.

Figure 4 shows the radio sources observed at 164 MHz during the initiation phase and labeled α , β and γ . All together, these sources trace a latitudinally broad coronal region, with an angular extend of ≈ 40 degrees, which overlies AR 9415 and AR 9417 visible on April 13 SOHO/MDI magnetogram (Figure 4, right panel). The $H\alpha$ flare (S20 W85) associated with the CME is marked with a yellow diamond for reference. On April 15, AR 9417 is well behind the limb, while AR 9415, is just at the limb. Sources α and β overlie the $H\alpha$ flare and AR 9417, respectively. Source γ is located at the vicinity of a preexisting noise storm. The first IP type III burst is associated with sources β - γ (Figure 4). The second IP type III burst is associated with sources α - γ . Finally, a weak IP burst is also detected at $\approx 13:42$ UT in association with sources α - β .

2.3. Impulsive Phase (13:45 - 13:48:30 UT)

This phase is characterized by an intense radio burst (Figure 1) and a strong increase of soft and hard X-ray fluxes (Figures 2, 3). Figure 5 shows a few snapshots of the 410 MHz source, called A_i during the *impulsive* phase of the event. The radio emission originates from two components: a sporadic component (labeled 'S' in Figure 5), produced by bursts of duration often shorter than 1 s, and a stable component, responsible for the continuum emission.

Nitta et al. (2003) reported *Yohkoh* soft X-ray telescope (SXT) observations of the flare and the faint loop-like structure, which appeared just at the onset of the impulsive phase of the flare at 13:45 UT, approximately

at the same time as the ejection of a bright helical structure seen by *TRACE* at 171 Å. This event closely followed the second IP type III burst observed by the NRH at 164 MHz by the end of the initiation phase (Figure 4). The location of the SXR source was found to coincide with the $H\alpha$ flare source (S20 W85). This location (yellow diamond) is reported in the snapshots on the right column of Figure 5. The A_i source is situated at a height $\approx 0.25R_\odot$ above the flare SXR source. It is well resolved at both 410 and 327 MHz and the positions coincide. The source has a relatively stable position during the impulsive phase (Figure 6). Its location is indicated by a white cross in the left panel of Figure 7.

Muraki et al. (2008) reported that the HXR source had a three-component structure, with two footpoints and one loop-top source in the energy channel 53-93 keV (see their Figure 23). Such HXR *loop-top* sources are present in a small fraction of impulsive flare events observed at the limb and are interpreted as evidence for magnetic reconnection (Masuda et al. 1994). An expanded view of the evolution with time of the HXR flux at 100-300 keV and of the radio emission at 327 MHz measured at a cadence of 1 s is shown in Figure 3. A similar evolution is seen at 432 and 410 MHz.

An outburst, starting at $\sim 13:47:30$ UT, is composed of type III bursts and of a weak coronal type II-like lane, also reported in Solar Geophysical Data (Figure 2). The 164 MHz observations place the origin of this event at ~ 1.15 - $1.3W$, $0.75S$, near the south edge of the radio CME (see blue triangles in the left panel of Figure 7). The above outburst was not detected at 236 MHz. Rather, at this frequency, a few bursts were detected between 13:48:00 UT and 13:48:20 UT (red triangles in the left panel of Figure 7). These bursts are located to the north and near the north edge of the radio CME when it is extrapolated back in time to the mean time of the bursts with constant velocity (dashed yellow line in Figure 7). Burst activity at 327 MHz was also detected between 13:47:50 and 13:48:20 UT at the north edge of the radio CME (green triangles). Other radio sources are detected at 236 MHz further north (red triangles in the left panel of Figure 7). An interpretation of these sources is proposed in Section 3.2.

2.4. Post-Impulsive Phase (13:48:30 - 14:20 UT)

2.4.1. Sporadic Sources and Radio CME

In the post-impulsive phase, the radio emission exhibits, first at the three highest NRH frequencies, a bursty component A superimposed on a smooth continuum (Figure 3). Source A moves outward (Figures 6, 7). Imaging at the highest cadence (125 ms) and at the 410 MHz frequency (close to the best resolving power of the NRH) allowed us to resolve the bursty radio emission into several episodes of sub-second bursts. To increase the contrast between the continuum and the bursts, an average background emission was subtracted: the background was taken as the mean value of the continuum emission during the 10 s preceding a group of bursts. With this background subtraction, the source measurements are obtained with an average signal-to-noise ratio ranging between 10 and 35. In each panel of Figure 8, the burst source is imaged at two times as indicated at the top of each panel. These examples show that during

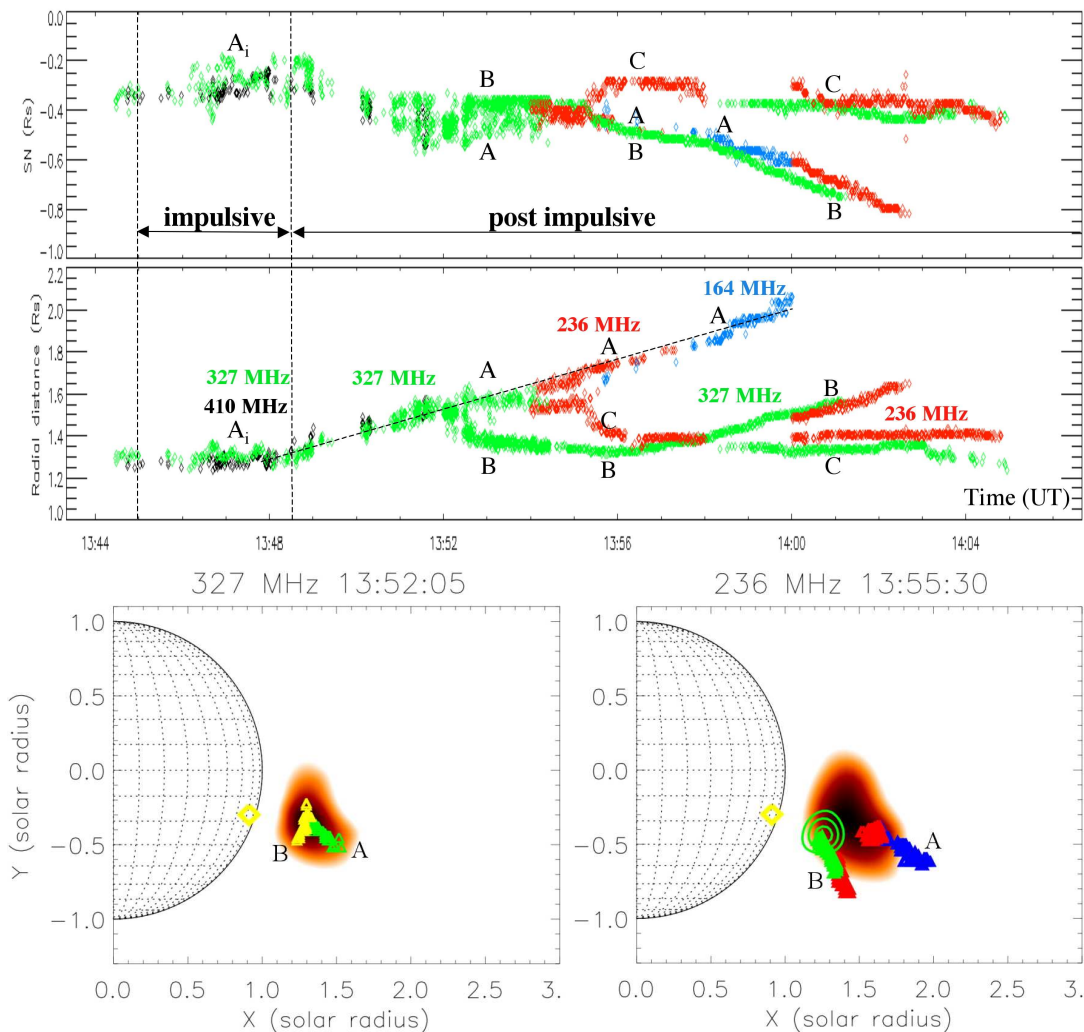


FIG. 6.— *Upper two panels*: time evolution of positions of the sources A (called A_i during the impulsive phase), B and C at 410 MHz (black), 327 MHz (green), 236 MHz (red) and 164 MHz (blue). The top panel shows the South-North position and the panel below shows the radial distance (selected because of a smaller overlap of the sources than with the East-West position). Note that at 410 and 327 MHz, the positions were measured with a cadence of 0.1s until 13:54:10 UT. All other positions were measured with a cadence of 1 s. *Lower left panel*: image of the source at 327 MHz measured at 13:52 UT. The downward motion at 327 MHz of source B (yellow) and of the simultaneous outward motion of source A (green) are reported during the time interval 13:52-13:56 UT. *Lower right panel*: image at 13:55:30 UT of the emissions at 236 MHz with iso-contours (green) at 327 MHz superposed. The motions after 13:55:30 UT of sources A and B are indicated by triangles (327 MHz: green; 236 MHz: red; 164 MHz: blue).

a time interval as short as 125 ms, the source structure can change drastically from one single component to two components located on either side of the single component.

More globally, the source A moves in the south-west direction with an emission drifting at lower frequency with time as expected for plasma emission with an outward motion (Figure 6). The dispersion of the points at 327 MHz is of the order of $0.1 R_\odot$, and is due to the presence of the distinct, short-lived, double components shown in Figure 8. A linear fit, reproduces well the global motion of source A. The derived apparent speed is ≈ 700 km/s and the global direction of the motion is reported in the two radio CME images in Figure 7 (yellow arrow).

Two other sources, B and C, detached successively from the back of source A, moving initially backward towards the Sun (as viewed in projection in the plane of the sky, Figure 6). The motions of the sources A and B are reported on the 327 and 236 MHz images in the lower panels of Figure 6. It is worth noting that the initial evo-

lution of the radial height, during about 4 min, of sources B and C is very similar: there is mainly a shift of time and of radial distance (middle panel of Figure 6). The difference in emission frequency is expected for plasma emission. Indeed source B emission shifts from 327 to 236 MHz as it moves out, while source C has the reverse shift as it moves closer to the Sun. The main difference between sources B and C is a difference in their motions later on: the outward speed of source B is ≈ 600 km/s while source C remains mostly stationary. Apart these differences, sources B and C have a similar global motion and relationship to source A. This indicates that they trace the same physical process, simply shifted in time and radial distance. The evolution of these sources is further analyzed in Section 4.2.

A radio CME was detected from 13:48:30 UT to 13:54:26 UT (Maia et al. 2007). The radio-loops started from a few tenths to more than $1 R_\odot$ above the solar limb. The high energy cut-off of the gyro-synchrotron emitting electrons was estimated to be of the order of

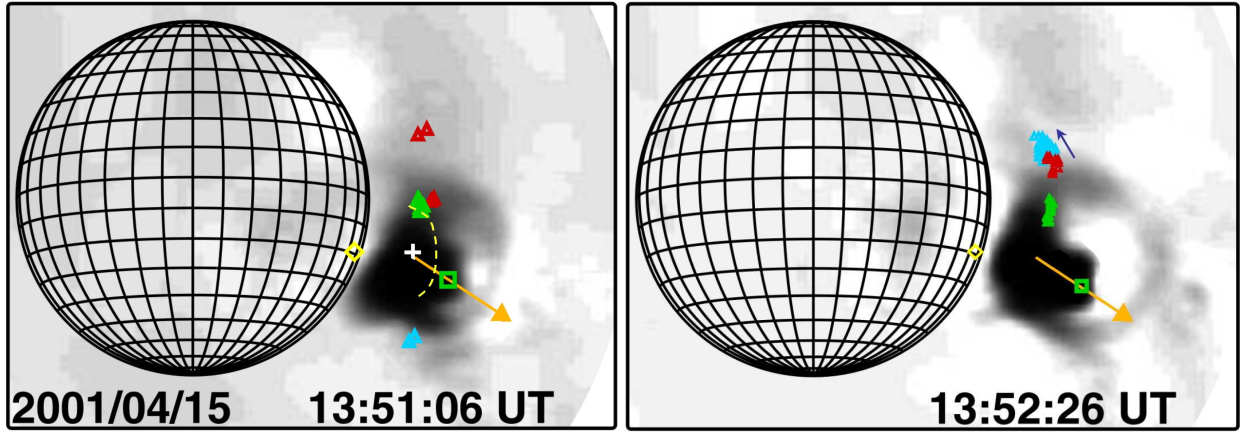


FIG. 7.— *Two images of the radio CME and related radio sources.* The green squares indicate the position of source A_1/A at the time indicated in the images and the yellow arrow the mean direction of motion (see Section 2.4.1). *Left panel:* origin of the first outburst starting at 13:47:30 UT and detected at 164 MHz (blue triangles, end of Section 2.3). The red/green triangles indicate the few weak bursts detected in the north at the same time at 236/327 MHz around 13:48-13:48:20 UT (same color coding of frequencies than in Figure 6). The white cross indicates the mean position of the source A_1 during the impulsive phase. The dashed yellow line represents the radio CME front extrapolated back in time, with a constant velocity, to the mean time of the radio bursts. *Right panel:* detection in the north of the outburst at 13:52 UT (Section 2.4.2) with the same color coding of the radio frequencies. The northward shift of the source is indicated by the blue arrow.

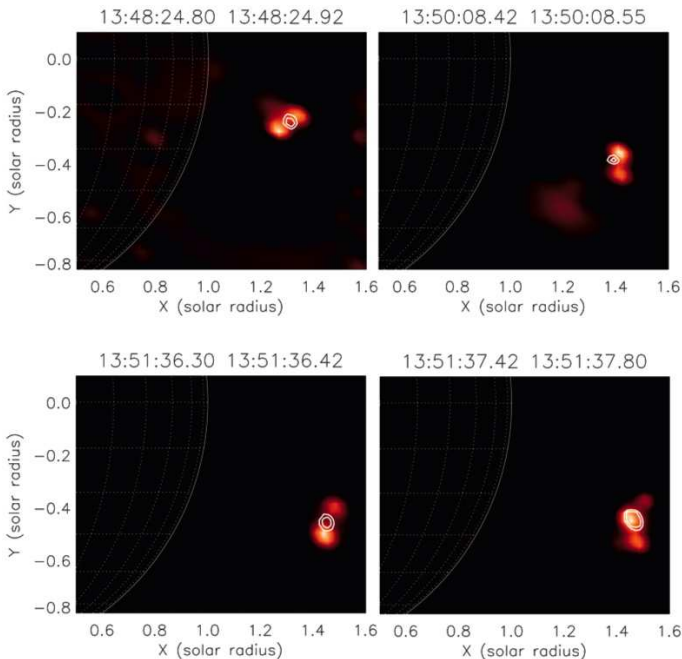


FIG. 8.— *Post impulsive phase:* snapshots of the emitting region at 410 MHz where the sources of the bursty emission are measured with a cadence of 125 ms and with the continuum emission subtracted. These sources, called globally 'A', often include two components. The source is imaged at two different times as indicated at the top of each panel. The contour plots correspond to the first time while the images correspond to the second one.

a few MeV, showing that electrons inside the loops and those detected in-situ by spacecraft at 1 AU had comparable energy. The radio CME was associated with the bursts seen in Figure 3 (top panel) above the continuum. After 13:52:30 UT, this bursty period stops and the continuum emission decreases slowly, whereas the radio CME becomes undetectable after 13:54:26 UT. Figure 7 shows at two distinct times the position of source A (green square) and the direction of its motion (yellow arrow), over the radio CME. The relationship of Sources A, B and C with the radio CME is further analyzed in Section 4.2.

2.4.2. Outbursts

We have already analyzed one outburst in Section 2.3. A second and third one, starting respectively at $\sim 13:51:10$ UT and at $\sim 13:52$ UT are shown in Figure 2. The second one is mainly composed of type III bursts; they are at the limit of detection at 164 MHz and their origin cannot be determined.

The third outburst includes a type II burst (see Solar Geophysical Data) and a series of strong IP type III bursts lasting for more than 20 minutes (Figure 2). The type II burst was also observed by WIND/WAVES but not detected below 0.7 MHz. This outburst presents all the characteristics of complex "type III like" emissions as defined by Reiner & Kaiser (1999). The outburst originates from the North, at $\sim 1.30W$, $0.20-0.25N$ (see red and blue triangles, at 236 and 164 MHz, in Figure 7, right panel). This emission was not detected after 13:53 UT at 236 MHz. At 164 MHz, the emitting source shifts progressively northward, from $0.25N$ at 13:53 UT to $0.38N$ at 13:55 UT (this displacement is indicated by the blue arrow in the left panel of Figure 7). This displacement corresponds to a projected velocity of ≈ 1000 km/s. The observations reveal that the type II/III bursts originate near the northern flank of the radio CME and could be produced by quasi-perpendicular coronal shocks and/or reconnection between the expanding CME and the surrounding magnetic structures.

2.4.3. Southern Expansion

In the latter phase of the eruption the radio sources have a tendency to drift southward (Figure 6). This is especially true for source B after $\sim 13:55$ UT and for source C after $\sim 13:58$ UT (a southward drift is also present for source A, but combined to its westward drift, source A moves closer to the radial direction, see Figure 11, top panel).

Later on, after 14:03 UT at 236 and 164 MHz, a striking feature is the occurrence of burst sources which drift progressively towards the south-east direction in contrast to the south-west motion of the CME. This source drift is shown at 236 and 164 MHz, superimposed on the im-

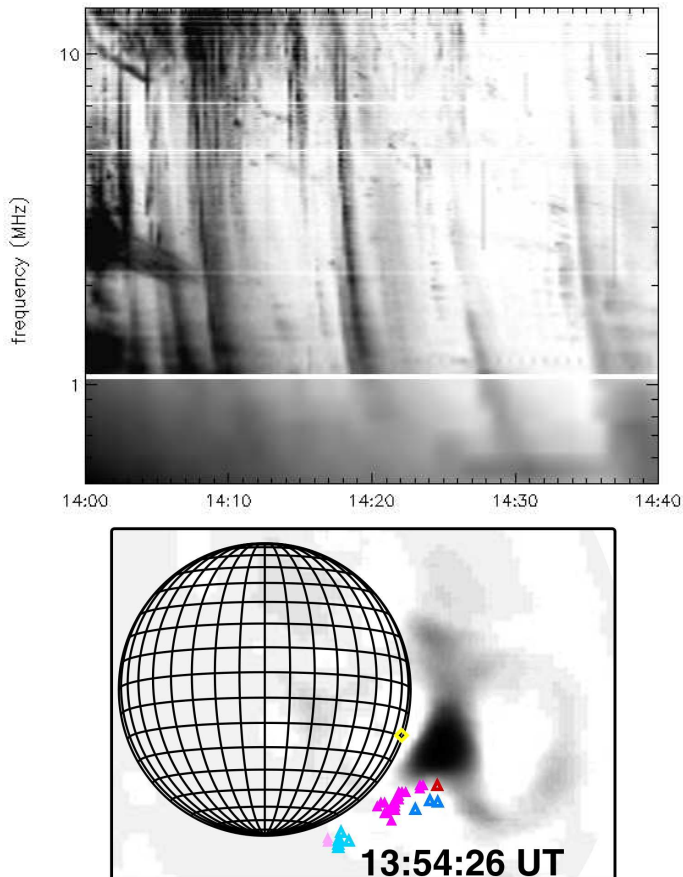


FIG. 9.— *Southern expansion.* *Top panel:* interplanetary type III bursts seen by WIND/WAVES. *Bottom panel:* successive locations of the burst source observed at 236 MHz (red/purple) and 164 MHz (blue) over plotted on the radio CME. The deep red color refers to the bursts observed at 13:59 UT. The purple and blue colors refer to the later period of 14:03 to 14:18 UT and the pink and light-blue color refer to the latest period 14:32-14:33 UT.

age of the radio CME at 13:54:26 UT, in Figure 9 (lower panel). After 14:20 UT the source reached a stable position. The IP counter parts of these sources are type III bursts seen by WIND/WAVES (Figure 9, top panel).

3. COMPARISON OF THE NRH TO THE EIT AND LASCO OBSERVATIONS

3.1. Radio and white light CME

Maia et al. (2007) discussed the close kinematical and morphological similarities between the radio and white light CME. They showed that the radio height-time measurements extrapolate well to the location of the CME front in C2 (Figure 4 in Maia et al. 2007) and noted the smaller extent of the radio CME relative to the white light event. They accounted for this discrepancy by surmising that only the southern part of the CME was illuminated in the radio waves. Our analysis suggests that the radio CME is actually the ejected flux rope and hence it occupies a smaller area than the overall white light CME which includes the shock and deflected streamers (e.g., Vourlidas & Ontiveros 2009).

To investigate, in more detail, the relation of the radio CME to its white light counterpart, we measured both the radial and lateral expansion of the radio CME. For this task, the position of the radio front was determined by eye, and we manually selected 13 data points along the radio front for each of the six frames in Figure 3 of

Maia et al. (2007). An error of $0.05 R_{\odot}$ was assumed. The selected points are plotted in Figure 10 (top panels) as crosses. We next used a spline interpolation to get 115 points across the front. The front of the radio CME has a rather clear elliptical shape, so we fitted an ellipse to those points and obtained the ellipse center, semi/major and semi/minor axes, and orientation as a function of time. Note that only the front of the radio CME is clearly visible in the images. The sunward part is obscured by the intense radio emissions from the current sheet and the post-flare loops. The lack of any data points at the back of the radio CME may have some effect on the precision of the ellipse center but the effect must be small since our data points cover about 3/4 of the overall radio CME and we are interested in the relative expansion of the CME front, not the overall volume.

Because of the small number of data points in time, a straight line fit (constant speed) is the simplest assumption (Figure 10, bottom panels). For the ellipse center, corresponding to the 'bulk' motion of the radio CME, the resulting speed is $\approx 1255 \pm 73$ km/s. The radial expansion speed (relative to the CME center) is given by the semiminor axis speed which is 277 ± 72 km/s which leads to a frontal speed of the radio CME of $\approx 1532 \pm 103$ km/s (the speed commonly derived for CMEs and used in catalogues). Correspondingly, the lateral expansion speed is $\approx 735 \pm 37$ km/s. Hence, the radio measurements quantify the visual observations that the CME is expanding laterally in its early stages. The lateral CME expansion is about 2.7 times larger than its radial expansion. We return to this point in the next section.

The above results refer to the evolution of the radio CME between 13:51:06 UT and 13:54:26 UT. We extrapolate these measurements to 14:06 UT, the time of the first observation in the C2 field of view. The result is the solid ellipse in Figure 10 (top panels) and the cross marks its center. The $\pm 1-\sigma$ ellipses are also plotted with dashed lines to provide an indication of the uncertainties in the extrapolation. Given the small number of radio measurements and the simple fitting process, the agreement between the radio CME and the flux rope white light structure is quite satisfactory. The extrapolated center of the radio CME coincides with the center of the white light flux rope cavity. The radio CME is clearly smaller than the white light CME which includes deflected streamers, clearly visible along the northern flank. We reach the same conclusion by re-analyzing the radio CME of Bastian et al. (2001) in a similar way than above.

3.2. Lateral interactions of the erupting flux rope

The radio emissions have an even broader lateral extension than the radio CME during both impulsive and post-impulsive phases (Figure 7). This broad lateral extension is also present in the initiation phase (Figure 4). The radio-emission extension is much broader than the AR source region, and we interpret it as the interaction/reconnection with surrounding magnetic structures. More specifically, we interpret the sources α - β at $\approx 13:42$ UT (Figure 4) as tracing energetic electrons in the magnetic connections between ARs 9415 and 9417. Indeed, their nearly parallel magnetic bipoles create opposite magnetic fields in between them, and as these ARs are expanding during their evolution (especially AR 9415 before it launched the CME), their magnetic configura-

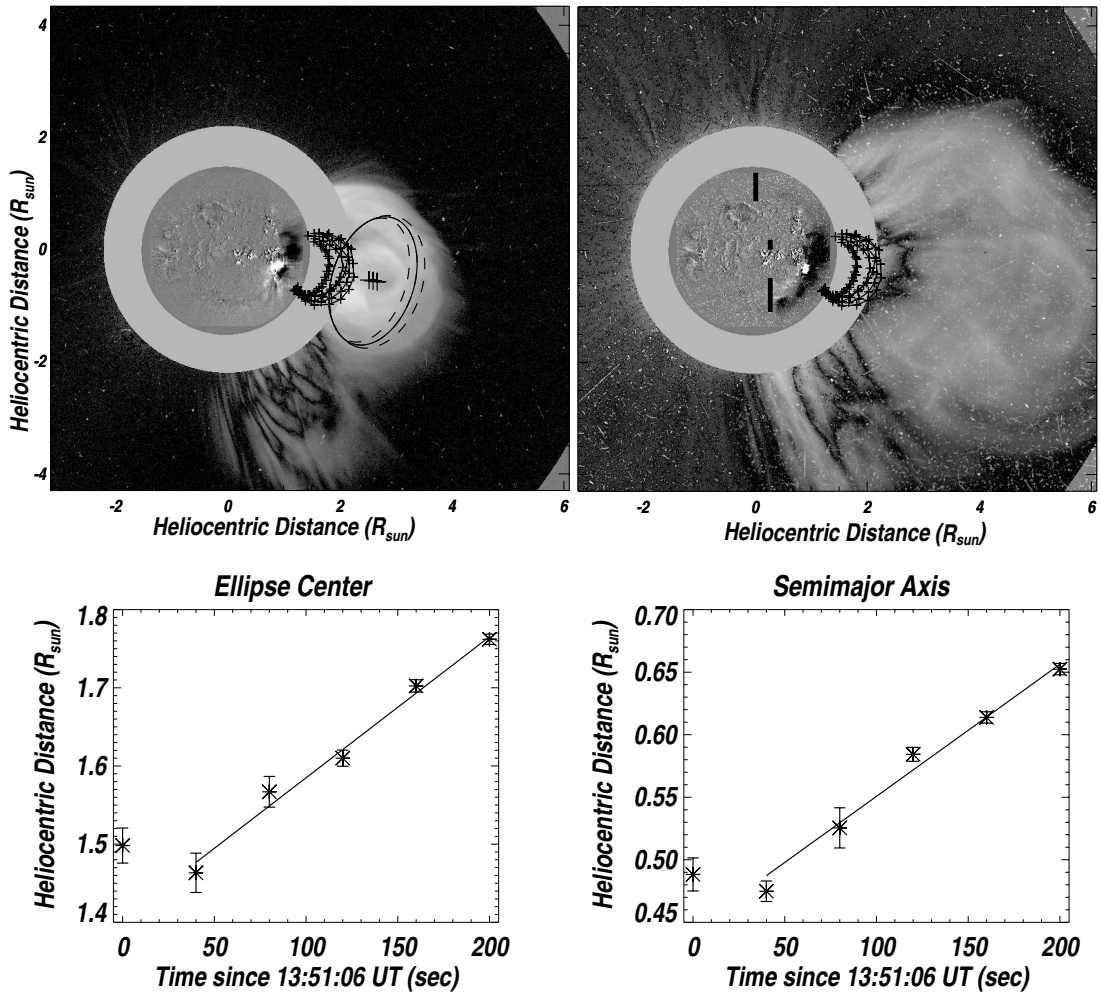


FIG. 10.— *Top panels*: LASCO/C2 images combined with EIT base difference images. The lines with crosses are the measured front of the radio CME in the NRH 410 MHz images between 13:51:06 and 13:54:26 UT (see images in Figures 7 and 9). *Top left panel*: C2 image at 14:06 UT and EIT base difference (14:12 - 13:48 UT). The CME is primarily expanding northward during this time as evidenced by the EIT dimmings. The solid ellipse marks the extrapolated location of the radio CME at the time of the C2 image (14:06 UT). The dashed ellipses denote the $\pm 1\text{-}\sigma$ uncertainty in the extrapolations of the fits shown in the bottom panels. *Top right panel*: C2 image at 14:30 UT and EIT base difference (14:24 - 13:48 UT). The CME dimmings have expanded considerably southwards since 14:06 UT. *Bottom panels*: evolution of the ellipse parameters (in R_{\odot}) versus time (in s) as fitted to the radio CME front.

tions are expected to partially reconnect. We also interpret the two type III bursts as due to reconnection of the growing AR 9415 with open magnetic fields. These reconnections also imply the formation of magnetic connections between AR 9415 and its surroundings, and imply a broad latitudinal extension of the magnetic structures already near the event onset (the observed extension $\approx 40^\circ$).

The interaction with the surrounding magnetic structure is further present as the CME expands in the impulsive and post impulsive phases. The CME certainly affects the loop system of AR 9417, as at least some of the eastern loops systems in AR 9417 disappeared in the EIT images, so the CME affected both ARs. We compare below the above latitudinal extension to the maximum lateral extent of the CME in white light. This extension is hard to judge due to the ever expanding streamers in the north and the lack of C2 images (only two are available). Still, the EUV dimming is quite stable after 14:12 UT so we use that as an indicator of the true width of the CME. In that case, the dimming extends to $\approx 60^\circ$ in position angle, which is comparable but still significantly larger than the angular extend of the radio sources dur-

ing the initiation phase.

The interaction of the CME with its surroundings is also observed by the NRH. We already described the type II bursts at the northern flank of the CME (Section 2.4.2). The EIT images allow us an independent estimate of the lateral expansion of the event by measuring the distance of the northernmost edge of the EUV dimming at 14:00 UT from the center of the flare. We estimate a lateral expansion speed of ≈ 900 km/s which is comparable to the northward speed of ≈ 1000 km/s of the sources observed at 164 MHz (Section 2.4.2) within error bars of the order of 100 km/s. These speeds are larger than the lateral expansion speed of the radio CME ≈ 735 km/s (Section 3.1).

Moreover, radio sources at 236 MHz are detected further north around 13:48 UT (Figure 7, left panel), well separated from the CME edge front. A northern radio extension, away from the radio CME loop structure, can also be clearly seen in the NRH 410 MHz images after about 13:53 UT (see Figure 3 in Maia et al. 2007). Such radio sources could be produced by electrons accelerated along large-scale loops connecting the CME source region to the northern hemisphere. More precisely, we propose

that the expanding flux rope reconnected with loops linking the negative polarity north-east of AR 9415 to the disperse positive polarity further northward (see the 13 April magnetogram in Figure 4). The electrons accelerated in the reconnected loops may be at the origin of the most northern radio sources (e.g. Maia et al. 1999).

The radio, EUV, and white light measurements also agree on the southward expansion of the CME. The combined EIT-LASCO observations at 14:30 UT show an EUV dimming extension to the south connected to a deflected streamer (Figure 10, right top panel). Note that the subtracted background for the LASCO images contains traces of a previous slow CME. The deflected streamer can be discerned in the image by its bright stalk at around 190° position angle. The radio sources, reported in Section 2.4.3 and Figure 9, occur at the boundary of the streamer as it is being deflected southwards. We conclude that these radio sources trace the southward interaction of the CME and its reconnection with the open field lines of opposite magnetic polarity (than the following polarity of the source AR, so of the closest flux rope footpoint). Then, such reconnection is at the origin of the observed IP type III bursts.

In summary, we can reconcile the similarities and difference between the white light, EUV and radio observations with the following interpretation. The radio CME is the expanding flux rope which is driving a density compression all along its front (while more important along its northern flank). The flux rope, traced by the radio CME, has a larger lateral than radial expansion in the corona. This lateral expansion drives a streamer pileup (seen in C2), and also a strong interaction with surrounding magnetic structures, likely involving shocks and magnetic reconnection. These are at the origin of the observed radio sources both northward and southward of the radio CME (seen in NRH) as well as the latitudinal extension of the EUV dimmings (seen by EIT).

4. INTERPRETATION OF OBSERVATIONS WITHIN PRESENT CME KNOWLEDGE

The radio and white light observations brought complementary informations on the physical processes involved in the CME. We discuss below the physical consequences within the present knowledge of CME initiation.

4.1. *Initiation and Impulsive Phases*

We interpret the preexisting noise storm and the increase of soft X-ray emission, in the initiation phase, as evidence of magnetic reconnection transforming the magnetic configuration of the AR. Indeed, this is only the final part of a preparation phase which progressively transforms magnetic arcades to a flux rope, a process which further inflates the magnetic configuration and leads to its interaction and reconnection with surrounding magnetic structures. Magnetic reconnection is expected to be active well before, during days, at the photospheric level with cancelation of small polarities. This process is presently well documented in several ARs observed close to central meridian (Green et al. 2011, and references therein). Of course, for the source AR of the studied CME, being at the limb, we could only argue that the same generic process was at work there. Then, the initiation phase occurred when part of the reconnection process shifted at the coronal level (due to a global up-

ward motion of the magnetic configuration as the flux rope is building up, see Aulanier et al. 2010, and references therein). Then, a part of the coronal radio sources (source α) and soft X-ray emissions are interpreted as a consequence of the magnetic energy release. Moreover, even prior to the impulsive phase, radio sources have a broad latitudinal extension. We interpret this as a consequence of the interaction/reconnection of the source AR with the surrounding and large-scale magnetic fields (Section 3.2).

The impulsive phase is characterized by a dramatic speed up of the coronal reconnection, which occurs on the time scale of minutes, as traced by radio flux evolution (Figure 1), and is probably bursty (as implied by the fast evolution, on time scale of 0.1 s, of the 'S' source in Figure 5). During and after this phase, photospheric reconnection is much too slow to have significant effect on the magnetic configuration. This fast coronal reconnection allows the release of an important part of the free magnetic energy contained in the highly sheared core field. High energy particles are at the origin of the X-ray and radio emissions observed above the flaring region (Figures 1,3,5). This reconnection further builds up the flux rope, as observed with sigmoidal loops formed above simple flare loops in several on disk ARs (Liu et al. 2010, and references therein).

The NRH imaging shows that for the April 15 2001 CME there is significant upward motion only by the end of the impulsive phase (Figure 6). The acceleration peak was indeed very short (less than one minute), and source A₁ changes from being nearly stationary to having a fast, nearly constant, speed ≈ 700 km/s later on (source A). The bulk speed of the flux rope, as traced by the radio CME, is significantly faster (≈ 1250 km/s). The ejection is expected to be due to a loss of equilibrium or a global instability driven by the hoop force (indeed both approaches are different views on the same physical mechanism, Démoulin & Aulanier 2010). This hoop force is present when a twisted flux tube has a curved axis. The electric current of a curved channel creates a magnetic field component orthogonal to the channel, and this implies an outward Laplace force (away from the curvature center). Magnetic reconnection is not needed in such initiation mechanism, but both radio and X-ray observations are indirect evidences that reconnection was already at work well before the ejection occurred. Indeed, on one hand magnetic reconnection further built up the flux rope before and during the ejection, so enhancing the hoop force. On the other hand, the upward motion of the flux rope induces a magnetic pressure depression behind, which drives inflows toward the reconnection region, enhancing the reconnection rate. Thus, a feedback between reconnection and the global outward instability is expected (see e.g. Zhang and Dere 2006; Maričić et al. 2007; Vršnak 2008).

4.2. *Post-Impulsive Phase*

Fast electrons are expected to be accelerated in the reconnection region, as well as within the turbulent reconnection jets and their associated shocks (if they are super Alfvénic). A fraction is injected in the reconnected loops below (flare-like loops) while the other part is injected in the new layer of reconnected field lines around the flux rope. Both set of electrons are expected to have

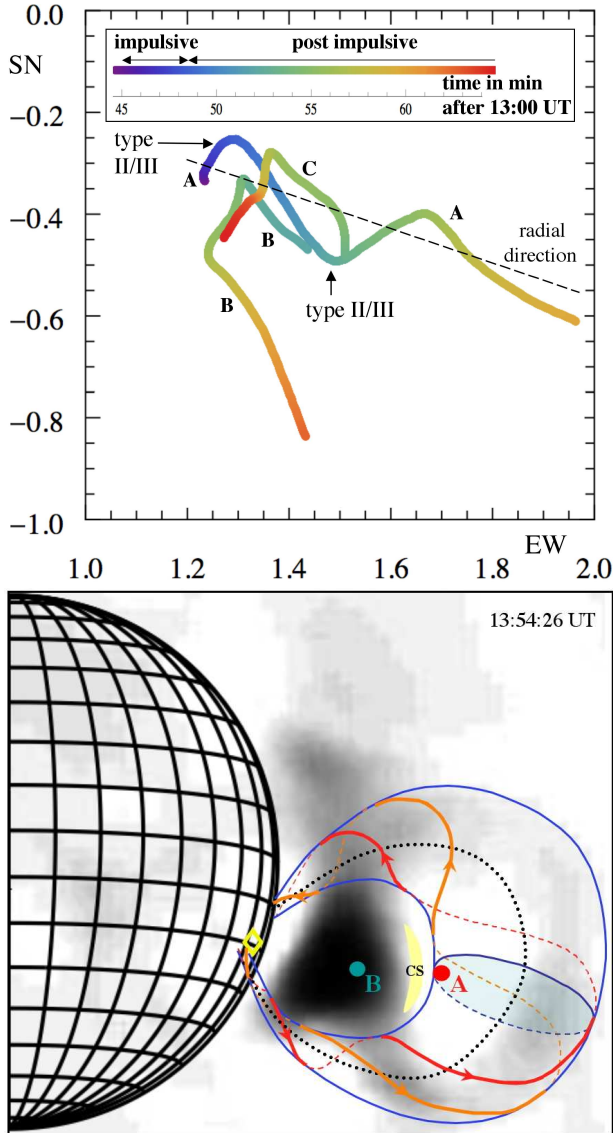


FIG. 11.— *Top panel*: spatial evolution of the radio sources A, B and C. The time is color coded as shown in the top caption. *Bottom panel*: spatial positions of the radio sources A, B and C compare to the radio CME observed at the same time. The expected shape of the eruptive flux rope is outlined in blue (the lower part points to the source AR and is in dashed since reconnection with the surrounding magnetic structures have probably occurred).

emissions detected at radio wavelengths. We then interpret source A as the signature of the upward injected electrons while sources B and C are associated to the downward injection in the standard model of an erupting flux rope (Forbes et al. 2006, and references therein). Then, sources A and B, C are expected to surround the current sheet formed below the erupting flux rope. The plasma emission of source A progressively shifts to lower frequency as the flux rope expands up in lower density regions. The plasma emission of source B or C is present at a given frequency only when the top of the reconnected loops is high enough in the corona, so that the local plasma frequency becomes lower than the observing frequency. Moreover, observing at a finite number of frequency induces the observing bias that the apparent downward moving sources occurred as discrete events (selecting the reconnected loops when they are in a range of density corresponding to the observed frequency, so

source B is observed as separated from source C).

Next we turn to a more detailed analysis of the source evolution. A summary of their spatial and temporal evolution is shown in the top panel of Figure 11. Source A has a global outward radial motion, but with abrupt changes in its moving direction. Corresponding changes of direction are present for sources B and C (when they are present). The first two changes are related temporally to the two type II/III bursts observed in the radio spectrum (Section 2.4.2 and Figure 2). These bursts are a trace of the southern and northern interactions of the CME with the surrounding magnetic structures (Figure 7). Such strong interaction is due to the fast lateral expansion of the CME (Section 3.2, Figure 10). We suggest that these lateral interactions, likely involving reconnection, have significant effect on the reconnection region located below the flux rope (as source A changed of moving direction at the times of the two type II/III bursts).

From Figure 11, it is striking to observe that both sources B and C follow mostly the same path than source A but backward and with a shift in time. This motion is indeed expected in the flux rope model where sources B and C trace the downward injected electrons while source A trace the upward injection. Furthermore, sources B and C have a similar evolution in the two first periods of time while they differ only in the last period of time, as follows (Figure 6). In the first phase they separate rapidly from source A with a downward motion of ≈ 3000 km/s for about half minute (after 13:52/13:55 UT for source B/C, respectively). In the second phase they continue their downward motion but with a slower motion of ≈ 230 km/s. Finally, in the last phase, source B move up with a velocity of ≈ 600 km/s while source C is approximately stationary.

It is tempting to interpret the first evolution phase, of the sources B and C, as the signature of the fast downward reconnection jet (see, e.g., Figure 1 of Forbes & Acton 1996). With this interpretation, the electrons would be accelerated within the turbulent jet of reconnection, so that the induced plasma emission would follow approximately the plasma motion. With a Mach number of 2, this would indicate an Alfvén velocity of 1500 km/s which is fast but of reasonable magnitude taking into account that this event is one of the largest event of its solar cycle, so that it involves much stronger magnetic fields than typical.

In the second phase, the downward motion is much slower. This motion could be associated to a displacement of the radio source along the curved base of the erupting flux rope. Then, in projection, it would show as a downward motion. However, it is not possible to quantify this effect as we have only 2D images of the CME. Given the large magnitude of the effect and the observed speeds we believe that a more plausible interpretation for the downward motion is the shrinkage of the reconnected loops (Forbes & Acton 1996). Indeed, this downward motion has a comparable magnitude than observed with UV and soft X-rays in supra-arcade downflows and supra-arcade downflowing loops which are observed as downflowing voids and bright loops, respectively, due to a different observing point of view (Savage et al. 2010; Savage & McKenzie 2011). These down flows are significantly slower than the expected velocity of reconnected

jets (of the order of the Alfvén velocity). The comparable velocity obtained between UV, soft X-rays and radio downflows is in favor of electron acceleration within these flows.

After the shrinkage phase, the third phase is likely to be dominated by the accumulation of reconnected loops. In this phase, the radio emission is not expected to follow a given loop top, but rather to trace the terminal shock, or at least the turbulent region, located above the accumulation of reconnected loops. This emission can stay relatively stable (source C) or even move up (source B). Finally, the southward motion of source B is expected to be related to the interaction, and probably reconnection, of the CME magnetic field with the southern fields (see Section 3.2).

Next, we turn to the spatial organization of the radio sources and CME. In Section 3.1, we found that the white-light front is larger than the radio CME. This is so because the coronagraph observations outline the denser region which is formed by the accumulated plasma around the expanding flux rope (“snow plow” effect). The radio CME rather shows the border of the flux rope, i.e. the last layer of magnetic flux which was reconnected behind the flux rope. Then, we are expecting to find source A at the lower bottom of the flux rope, while sources B and C at the top of the reconnected loops. Figure 11, bottom panel, show the source positions when they are the most separated while the radio CME is still observed. Source B is well inside the strong radio emission which is expected to be emitted within the reconnected loops. We have no observational constraint for the location of the flux rope lower boundary. Rather, within the above theoretical framework, we set the source A just above this lower boundary. With the front boundary defined by the radio CME and the AR source region, we then define the probable extension of the flux rope (outlined by blue lines and two twisted field lines in Figure 11). It implies that the flux rope is highly inclined along the line of sight (as indicated by the shaded cross-section), which is in agreement with the dominantly north-south orientation of the AR magnetic inversion line (Figure 4) as well as the EUV dimming orientation (Figure 10, top panels). This conclusion contrasts with the intuitive conclusion that could be reached by only seeing the radio CME: since it has a globally round shape we could be tempted to conclude that the radio CME trace the cross section of the an east-west oriented flux rope (for example as the CME analyzed by Chen et al. 1997). However, even highly-inclined flux ropes can appear circular in projection (Vourlidas et al. 2011). Moreover, the 2001 April 15 CME has the typical flux rope orientation expected for a CME located at the south-west limb (Cremades & Bothmer 2004), and the flux rope is rather observed from the side.

Finally, the lateral extension of the CME and its interaction/reconnection with surrounding magnetic regions was present already in the pre-eruptive phase (Figure 4), but also in the impulsive and post-impulsive phases (Figure 7) as analyzed in Section 3.2. Later on this interaction further developed, especially toward the southern pole, as traced by radio sources (Figure 9). This is a classical observations for large events which are observed to become large scale, not only by lateral expansion, but also by reconnection with the surrounding structures (see

Section 1 and the review of van Driel-Gesztelyi et al. 2008). This multiple reconnections with large scales, in particular open field, allows the access for energetic particles to a broad range of IP structures (as traced by type III bursts). A much deeper analysis of the type of reconnection implied in such broad injection range is provided in Masson et al. (2012b).

5. CONCLUSIONS

We used the images acquired on April 15 2001 by the Nançay Radioheliograph and SOHO EUV and coronagraph instruments to investigate the relation of the radio CME to its EUV and white light counterpart. In the following, we summarize the most important finding of our study:

- The radio CME corresponds to the flux rope seen in white light (Figure 10). Indeed, (a) the radio CME size is smaller than the white light CME which also includes compressed coronal plasma, in particular deflected streamers (visible along the northern flank); (b) its extrapolated center coincides with the center of flux rope cavity (observed in white light). We reach the same conclusion by re-analyzing the radio CME on 20 April 1998 of Bastian et al. (2001) in a similar way than above.

- The formation and reconnection of a current sheet, behind the erupting flux rope, provides a coherent interpretation of the spatial and dynamical behavior of the different radio sources detected behind the radio CME (Figures 6 and 11). These radio sources provide signatures of upward and downward injected electrons accelerated in the reconnection region and its outflows, as present within the standard model of an erupting flux rope (Forbes et al. 2006). The plasma emission associated with the upward electrons (source A) progressively shifts to lower frequency as the flux rope reaches lower density (Figure 6). The downward motion (of sources B and C) has three successive phases: the first one suggests a super Alfvénic downward reconnection jet, the second one is interpreted as the shrinkage of the reconnected loops (Forbes & Acton 1996; Savage & McKenzie 2011) and the third one corresponds to the accumulation of reconnected loops.

- Both Bastian et al. (2001) and Maia et al. (2007) attributed the faint emission of the radio CMEs to incoherent synchrotron emission from a few MeV electrons spiraling within a magnetic field ranging from 0.1 to a few gauss. In the present event, the current sheet, as traced by radio sources, is already well developed at $\approx 13:51$ UT, i.e. at the time of the first radio CME image. Within a fraction of second, the structure of the bursty source change abruptly from a single to two components located on each side of the former source (Figure 8). These observations suggest a dynamic phase of repeated magnetic reconnections which are accelerating nonthermal electrons. These high energy electrons are expected to be injected along the field lines that wrap around the flux rope and down along the reconnected coronal loops (see e.g. Zharkov et al. 2011).

- The spatial organisation of the radio CME and sources leads to the conclusion that the flux rope is highly inclined along the line of sight (Figure 11). This orientation is similar to the dominantly north-south orientation of the AR 9415 magnetic inversion line and of the EUV dimming. This conclusion contrasts with the intuitive

conclusion that could be reached by only seeing the radio CME: since it has a globally round shape we could be tempted to conclude that the radio CME trace the cross section of an east-west oriented flux rope.

- Already in the pre-eruptive phase, observed radio sources have a broad latitudinal extension ($\approx 40^\circ$), while smaller than the maximum CME extension ($\approx 60^\circ$) as traced by EUV dimmings later on (Figures 4 and 10).

- Radio images reveal an important lateral over-expansion in the low corona of the radio CME measured during the first 5 minutes and corresponding to a lateral/radial expansion velocity ratio of ≈ 2.7 (the expansion velocities are defined relative to the center of the CME, Figure 11). This over-expansion is at the origin of the build up of compression regions on the edges of the cavity which leads to the formation of coronal shocks and field line reconnections with the surrounding magnetic field (Yan et al. 2006). Indeed, during all the CME phases, radio observations provide evidence of interaction/reconnection of the flux rope with surrounding magnetic structures (Figures 2, 4, 7, 9). Moreover, this early over expansion is coherent with the CME shape seen later on in white light.

This CME demonstrates clearly the complementarity

of radio, EUV and white light observations. Radio observations are able to trace the very early interactions of the erupting magnetic structures and the consequences of reconnection behind the erupting flux rope. EUV traces the source region and the extension of the, so-called, opened field regions. Finally white light coronagraphic images trace the later development of the CME and its interaction with the surroundings.

Acknowledgements

The authors thank the referee for helpful comments which improved the clarity of the paper. One of the authors, M.P., is grateful to Dr Tim Bastian for his helpful criticisms during an important phase of this study. HXR count rates measured by Yohkoh were courtesy of A. J. Tylka and of the Yohkoh team. We are grateful to G. Trotter for his helpful comments. A. Vourlidas is supported by various NASA grants. In France, this work was supported by CNES. The SOHO/LASCO data used here are produced by a consortium of the Naval Research Laboratory (USA), Max-Planck-Institut für Aeronomie (Germany), Laboratoire d'Astronomie Spatiale (France), and the University of Birmingham (UK). SOHO is a project of international cooperation between ESA and NASA.

REFERENCES

- Amari, T., Aly, J.-J., Mikic, Z., & Linker, J. 2010, *ApJ*, 717, L26
 Attrill, G. D. R., Harra, L. K., van Driel-Gesztelyi, L., & Démoulin, P. 2007, *ApJ*, 656, L101
 Aulanier, G., Török, T., Démoulin, P., & DeLuca, E. E. 2010, *ApJ*, 708, 314
 Aurass, H., Landini, F., & Poletto, G. 2009, *A&A*, 506, 901
 Bastian, T. S., Pick, M., Kerdraon, A., Maia, D., & Vourlidas, A. 2001, *ApJ*, 558, L65
 Bougeret, J.-L., Kaiser, M.L., Kellogg, P.J., Manning, R., Goetz, K., et al. 1995, *Space Science Reviews*, 71, 231
 Brueckner, G. E., Howard, R. A., Koomen, M. J., Korendyke, C.M., Michels, D.J., et al. 1995, *Sol. Phys.*, 162, 357
 Chen, J., Howard, R. A., Brueckner, G. E., Santoro, R., Krall, J., et al. 1997, *ApJ*, 490, L191
 Chen, P. F. 2011, *Living Reviews in Solar Physics*, 8, 1
 Cheng, X., Zhang, J., Liu, Y., & Ding, M. D. 2011, *ApJ*, 732, L25
 Ciaravella, A., & Raymond, J. C. 2008, *ApJ*, 686, 1372
 Cohen, O., Attrill, G. D. R., Schwadron, N. A., Crooker, N.U., Owens, M.J., Downs, C., Gombosi, T.I. 2010, *J. Geophys. Res.*, 115, A10104
 Cremades, H., & Bothmer, V. 2004, *A&A*, 422, 307
 Delaboudinière, J.-P., Artzner, G. E., Brunaud, J., Gabriel, A. H., Hochedez, J. F., et al. 1995, *Sol. Phys.*, 162, 291
 Démoulin, P., & Aulanier, G. 2010, *ApJ*, 718, 1388
 Forbes, T. G., & Acton, L. W. 1996, *ApJ*, 459, 330
 Forbes, T. G., Linker, J.A., Chen, J., Cid, C., Kóta, J., et al. 2006, *Space Sci. Rev.*, 123, 251
 Green, L. M., Kliem, B., & Wallace, A. J. 2011, *A&A*, 526, A2
 Hood, A. W., Archontis, V., Galsgaard, K., & Moreno-Insertis, F. 2009, *A&A*, 503, 999
 Huang, J., Démoulin, P., Pick, M., Auchère, F., Yan, Y.H., Bouteille, A. 2011, *ApJ*, 729, 107
 Illing, R. M. E., & Hundhausen, A. J. 1986, *J. Geophys. Res.*, 911, 10951
 Karlický, M., Fárník, F., & Krucker, S. 2004, *A&A*, 419, 365
 Kerdraon, A., & Delouis, J.-M. 1997, *Coronal Physics from Radio and Space Observations, Lecture notes in Physics*, 483, 192
 Kliem, B., Karlický, M., & Benz, A. O. 2000, *A&A*, 360, 715
 Lin, J., & Forbes, T. G. 2000, *J. Geophys. Res.*, 105, 2375
 Liu, R., Liu, C., Wang, S., Deng, N., & Wang, H. 2010, *ApJ*, 725, L84
 Luoni, M. L., Démoulin, P., Mandrini, C. H., & van Driel-Gesztelyi, L. 2011, *Sol. Phys.*, 270, 45
 Maia, D., Vourlidas, A., Pick, M., Howard, R., Schwenn, R., & Magalhães, A. 1999, *J. Geophys. Res.*, 104, 12507
 Maia, D. J. F., Gama, R., Mercier, C., Pick, M., Kerdraon, A., & Karlický, M. 2007, *ApJ*, 660, 874
 Mandrini, C. H., Nakwacki, M. S., Attrill, G., van Driel-Gesztelyi, L., Démoulin, P., Dasso, S., Elliott, H. 2007, *Sol. Phys.*, 244, 25
 Marčić, D., Vršnak, B., Stanger, A. L., Veronig, A.M., Temmer, M., et al. 2007, *Sol. Phys.*, 241, 99
 Masson, S., Démoulin, P., Dasso, S., Klein, K.-L., 2012a, *A&A*, 538, A32
 Masson, S., Aulanier, G.,ariat, E., Klein, K.-L., 2012a, *Sol. Phys.*, 276, 199
 Masuda, S., Kosugi, T., Hara, H., Tsuneta, S., & Ogawara, Y. 1994, *Nature*, 371, 495
 Muraki, Y., Matsubara, Y., Masuda, S., Sakakibara, S., Sako, T., et al. 2008, *Astrop. Phys.*, 29, 229
 Nitta, N. V., Cliver, E. W., & Tylka, A. J. 2003, *ApJ*, 586, L103
 Patsourakos, S., Vourlidas, A., & Kliem, B. 2010, *A&A*, 522, A100
 Pick, M., Démoulin, P., Krucker, S., Malandraki, O., & Maia, D. 2005, *ApJ*, 625, 1019
 Pick, M., & Vilmer, N. 2008, *A&A Rev.*, 16, 1
 Pohjolainen, S., Maia, D., Pick, M., Vilmer, N., Khan, J.I., et al. 2001, *ApJ*, 556, 421
 Reiner, M. J., & Kaiser, M. L. 1999, *Geophys. Res. Lett.*, 26, 397
 Saint-Hilaire, P., Krucker, S., & Lin, R. P. 2009, *ApJ*, 699, 245
 Savage, S. L., McKenzie, D. E., Reeves, K. K., Forbes, T. G., & Longcope, D. W. 2010, *ApJ*, 722, 329
 Savage, S. L., & McKenzie, D. E. 2011, *ApJ*, 730, 98
 Subramanian, P., & Vourlidas, A. 2007, *A&A*, 467, 685
 Thernisien, A., Vourlidas, A., & Howard, R. A. 2009, *Sol. Phys.*, 256, 111
 Tylka, A. J., Cohen, C.M.S., Dietrich, W.F., Krucker, S., McGuire, R.E., et al. 2003, *International Cosmic Ray Conference*, 6, 3305
 van Driel-Gesztelyi, L., Attrill, G. D. R., Démoulin, P., Mandrini, C. H., & Harra, L. K. 2008, *Annales Geophysicae*, 26, 3077
 Vourlidas, A., & Ontiveros, V. 2009, *Amer. Inst. of Phys. Conf. Ser.*, 1183, 139
 Vourlidas, A., Colaninno, R., Nieves-Chinchilla, T., & Stenborg, G. 2011, *ApJ*, 733, L23
 Vršnak, B. 2008, *Annales Geophysicae*, 26, 3089
 Vršnak, B., Poletto, G., Vujić, E., Vourlidas, A., Ko, Y.-K., et al. 2009, *A&A*, 499, 905
 Yan, Y., Pick, M., Wang, M., Krucker, S., & Vourlidas, A. 2006, *Sol. Phys.*, 239, 277
 Zhang, J., Dere, K. P., Howard, R. A., Kundu, M. R., & White, S. M. 2001, *ApJ*, 559, 452
 Zhang, J., & Dere, K. P., 2006 *ApJ*, 649, 1100

Zharkov, S., Green, L. M., Matthews, S. A., & Zharkova, V. V.
2011, ApJ, 741, L35